

SparseDet: A Simple and Effective Framework for Fully Sparse LiDAR-based 3D Object Detection

Lin Liu, Ziyang Song, Qiming Xia, Feiyang Jia, Caiyan Jia, Lei Yang, Hongyu Pan

Abstract—LiDAR-based sparse 3D object detection plays a crucial role in autonomous driving applications due to its computational efficiency advantages. Existing methods either use the features of a single central voxel as an object proxy, or treat an aggregated cluster of foreground points as an object proxy. However, the former lacks the ability to aggregate contextual information, resulting in insufficient information expression in object proxies. The latter relies on multi-stage pipelines and auxiliary tasks, which reduce the inference speed. To maintain the efficiency of the sparse framework while fully aggregating contextual information, in this work, we propose SparseDet which designs sparse queries as object proxies. It introduces two key modules, the Local Multi-scale Feature Aggregation (LMFA) module and the Global Feature Aggregation (GFA) module, aiming to fully capture the contextual information, thereby enhancing the ability of the proxies to represent objects. Where LMFA sub-module achieves feature fusion across different scales for sparse key voxels via coordinate transformations and using nearest neighbor relationships to capture object-level details and local contextual information, GFA sub-module uses self-attention mechanisms to selectively aggregate the features of the key voxels across the entire scene for capturing scene-level contextual information. Experiments on nuScenes and KITTI demonstrate the effectiveness of our method. Specifically, on nuScene, SparseDet surpasses the previous best sparse detector VoxelNeXt by 2.2% mAP with 13.5 FPS, and on KITTI, it surpasses VoxelNeXt by 1.12% AP_{3D} on hard level tasks with 17.9 FPS.

Index Terms—3D object detection, sparse detectors, feature aggregation

I. INTRODUCTION

3D object detection is a critical task in autonomous driving, promoting the advances of intelligent transportation systems, and has gained widespread attention [1]–[15]. With the availability of various sensor modalities, such as cameras and LiDAR, significant progress has been made in single-modal 3D object detection using either camera images [16]–[20] or LiDAR point clouds [21]–[23]. Compared to the image data provided by cameras, LiDAR point clouds offer accurate depth

This work was supported by the National Key R&D Program of China (2018AAA0100302). (Corresponding author: Caiyan Jia.)

Lin Liu, Ziyang Song, Feiyang Jia, Caiyan Jia are with School of Computer and Information Technology, Beijing Key Lab of Traffic Data Analysis and Mining, Beijing Jiaotong University, Beijing 100044, China (e-mail: 22110110@bjtu.edu.cn; liulin010811@gmail.com; cyjia@bjtu.edu.cn.)

Qiming Xia is with Fujian Key Laboratory of Sensing and Computing for Smart Cities, Xiamen University, Xiamen, China, Fujian 100044, China (e-mail: 22110110@bjtu.edu.cn; liulin010811@gmail.com; cyjia@bjtu.edu.cn.)

Lei Yang is with the State Key Laboratory of Intelligent Green Vehicle and Mobility, and the School of Vehicle and Mobility, Tsinghua University, Beijing 100084, China (e-mail: yanglei20@mails.tsinghua.edu.cn).

Hongyu Pan is with Horizon Robotics (e-mail: karry.pan@horizon.cc).

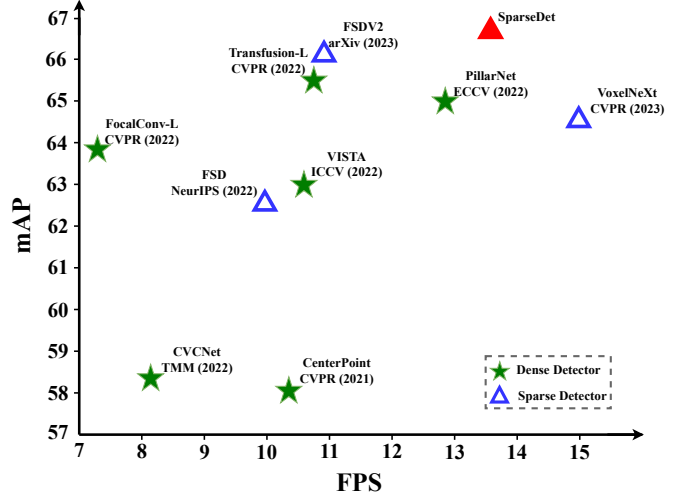


Fig. 1: The comparison of SparseDet with existing LiDAR-based detectors on nuScenes [32] test dataset, where the vertical axis represents mAP, and the horizontal axis represents model inference speed (FPS). Compared to other sparse detectors, SparseDet achieves the highest mAP while maintaining an excellent inference speed.

and position information and have led to extensive research in recent years [24]–[31].

Existing high-performance 3D object detectors [25], [37]–[39] typically leverage 3D sparse CNNs to extract features from sparse voxels, and then convert these features into dense feature maps for detection. Although these methods [37], [38], [40] have demonstrated impressive detection accuracy on a range of benchmark datasets [32], [41]–[43], extending them to more practical long-range scenarios becomes challenging. This is because the computational costs associated with the dense feature mappings grow quadratically as the perception range increases. Therefore, some recent works [33]–[36] have attempted to construct fully sparse detectors to cope with this issue.

Currently, based on the strategy of object proxies, LiDAR-based sparse detectors can be categorized into two distinct classes. The first category (e.g., [35], [36]) employs stacked convolutional layers to propagate sparse features to central voxels, which are then utilized as object proxies for detection. The second category (e.g., [33], [34]) aggregates foreground points into clusters and treats them as object proxies. Although the aforementioned methods have successfully constructed fully sparse detectors, the first category only treats individual

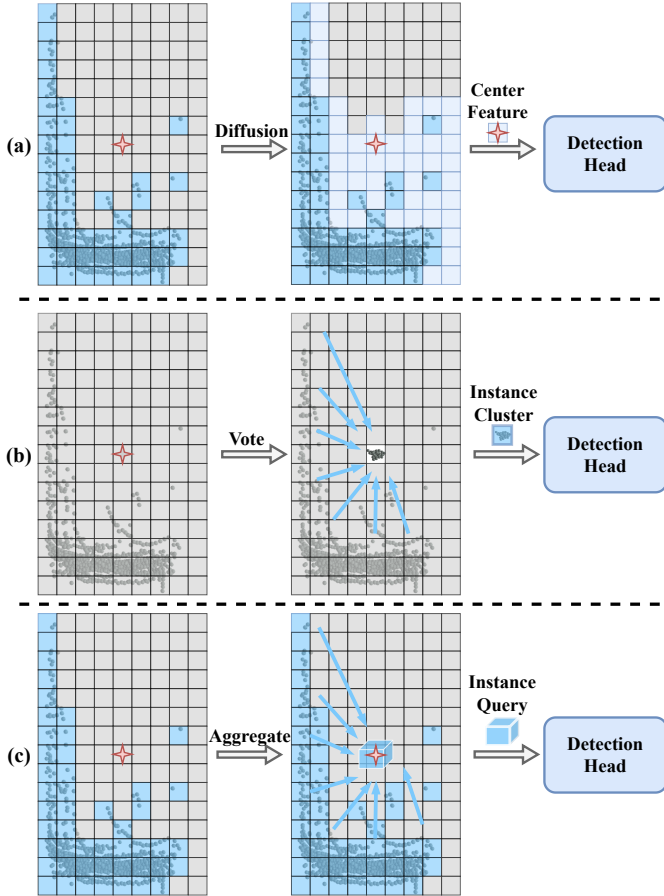


Fig. 2: **Comparison between SparseDet and other sparse detection frameworks [33]–[36].** (a) The first category methods, VoxelNeXt [35] and SAFDNet [36], diffuse feature by stacking convolutional layers to fill center voxels. However, utilizing only a single central voxel feature as a proxy for an object neglects an amount of instance features, thereby weakening the ability to represent objects based on their central voxels. (b) The second category method, FSD [33] and FSDV2 [34], utilize a voting mechanism to aggregate foreground points into object-centered clusters for further prediction. However, these methods overly relies on point segmentation and prediction refinement which results in time delays. (c) Our SparseDet addresses the issue of insufficient information representation in central voxel features by utilizing sparse queries as object proxies and selectively aggregating sparse voxel features at interested positions, avoiding the need for additional auxiliary tasks.

central voxels as object proxies, lacking the ability to learn point cloud context. This weakens the information representation capacity of object proxies. As shown in Fig. 2 (a), treating only the central voxel features as object proxies leads to the loss of some point cloud information from the same instance. The second category clusters foreground points into object-centric clusters for further prediction. As shown in Fig. 2 (b), it (e.g., [33] or [34]) initially segments the raw point cloud into foreground and background regions, performs center voting for instance clustering, then extracts instance features from

each cluster for initial predictions. Although these methods possess contextual aggregation capabilities, they heavily rely on additional auxiliary tasks and numerous hyperparameters, resulting in poor inference speed.

In order to achieve efficient detection while effectively aggregating contextual information in sparse frameworks, in this study, we propose a simple and effective fully sparse 3D object detection framework called SparseDet. SparseDet utilizes a 3D sparse convolutional network to extract features from point clouds and transforms them into 2D sparse features for further prediction via detection head. As shown in Fig. 2 (c), SparseDet designs sparse queries as object proxies, allowing to flexibly and selectively aggregate point clouds to obtain object proxies in a scene. Compared to the previous sparse aggregation paradigm [33], [34], firstly, SparseDet extends the aggregation of local contextual information to multi-scales feature space, thereby obtaining richer local information. Furthermore, in contrast to prior methods [33], [34] that only focus on aggregating foreground point features, SparseDet can aggregate the scene-level context for each instance to facilitate potential collaboration between the scene and instance features. Finally, SparseDet does not require any additional auxiliary task.

In order to enhance SparseDet’s ability to learn point cloud context, we have designed two key modules, the Local Multi-scale Feature Aggregation (LMFA) module and the Global Feature Aggregation (GFA) module. The LMFA module is aimed to capture local contextual information at multiple scales by only leveraging simple coordinate transformations and voxel’s nearest-neighbor relationships to collect features from neighboring key voxels. These features are then aggregated to obtain richer local representations. By these operations, LMFA module enables SparseDet to capture fine-grained details and local variations in point clouds. This enhances the expressive power of sparse queries and enables better representation of the underlying structures within point clouds. Afterwards, we initialize the aggregated features of the key voxels as sparse queries and feed them into GFA module. GFA module targets to aggregate global point cloud information across the entire scene by utilizing global sparse queries in a larger receptive field. This allows SparseDet to have a comprehensive understanding of the scene and incorporates global context into the detection process. Benefiting from the comprehensive learning of contextual information, SparseDet significantly enhances the information representation capability of object proxies and demonstrates superior performance (please see Fig. 1 as a reference).

We conduct extensive experiments on two popular datasets KITTI [41] and nuScenes [32] to verify the effectiveness of our method. Compared to the most of state-of-the-art (SOTA) methods, SparseDet demonstrates superior performance. Specifically, on the large-scale nuScenes dataset, SparseDet achieves a 2.2% improvement in mAP compared to the baseline model VoxelNeXt. And on KITTI SparseDet, it surpasses VoxelNeXt by 1.12% AP_{3D} on hard level tasks. Significantly, this performance enhancement is accomplished without introducing substantial additional latency. While achieving better performance than FSDV2, SparseDet

attains an FPS of 13.5, which is 1.38 times faster than FSDV2.

II. RELATED WORK

A. LiDAR-based Dense Detectors

Although point cloud data exhibits different sparsity characteristics compared to 2D image data, 3D object detectors are often designed by referencing 2D detectors. For example, most works [25], [26], [37], [44]–[46] have utilized 2D dense detection heads to address the problem of 3D detection. These methods are usually called LiDAR-based dense detectors [36].

As a pioneer, VoxelNet [26] partitions point clouds into regular grids and utilizes a 3D backbone network for feature extraction. It then applies a dense head for prediction. Based on VoxelNet, SECOND [25] implements efficient computation of sparse convolution and submanifold convolution operators to gain fast inference speed by constructing a hash table. However, SECOND still requires dense Bird’s Eye View (BEV) feature maps and dense detection head for detection. On the influence of SECOND, most subsequent networks [37], [44], [45], [47]–[50] follow the paradigm of utilizing a 3D sparse backbone combined with a 2D dense detection head.

Although LiDAR-based dense detectors have shown excellent performance on multiple benchmark datasets [32], [41]–[43], their reliance on dense Bird’s Eye View (BEV) feature maps and dense detection heads makes them be challenging to scale-up to long-range scene detection. This is because the computational costs of dense BEV feature map increases quadratically with detection distance [33]. This drawback significantly restricts the practical applications of LiDAR-based dense detectors in real-world scenarios.

B. LiDAR-based Sparse Detectors

Currently, sparse detectors include point-based methods and partial voxel-based methods. Point-based methods [27], [28], [51], [52] utilize key points within point clouds for feature aggregation and detection. These methods do not require dense sampling and computation across the entire space, making them inherently sparse detectors. FSD [33] and FSDV2 [34] are representative of this series of methods. FSD represents individual objects by clustering segmented foreground points. It then fed features which are extracted by PointNet into a detection head for calibration and prediction. In FSDv2, the instance clustering step is replaced with a virtual voxelization module, which aims to remove the inherent bias introduced by manually crafted instance-level representations. Despite adequately aggregating foreground information, the reliance on additional auxiliary tasks and numerous hyperparameters leads to poor inference speed.

Among the voxel-based sparse methods, VoxelNeXt [35] introduces additional downsampling layers to place voxels near the centers of objects and subsequently performs feature diffusion on key voxels to propagate features towards the object centers. SAFDNet [36] addresses the issue of missing central features by proposing an adaptive feature diffusion strategy. Although SAFDNet [36] and VoxelNeXt [35] have achieved impressive efficiency, they solely rely on single center voxel features for detection, which significantly weakens

the information representation capability of object proxies, ultimately leading to a decline in model performance. As mentioned before, treating only the central voxel features as object proxies leads to the loss of some point cloud information from the same instance as illustrated in Fig. 2 (a). In this work, we use sparse queries and attention mechanism to obtain object proxies by LMFA and GFA modules, which enable to dynamically capture contextual information at different granularities. This promotes the collaboration between scene-level and instance-level features, thereby enabling the model to obtain richer and more accurate object representations.

III. SPARSEDET

In this section, we propose a simple and efficient LiDAR-based sparse detection framework SparseDet. Fig. 3 illustrates its structure which follows the pipelines of the fully sparse network VoxelNeXt [35]. But differently, in order to fully aggregate the contextual information in point clouds to enhance the information expression capability of the sparse object proxies, we design two sub-modules, LMFA (Local Multi-scale Feature Aggregation) module and GFA (Global Feature Aggregation) module. The two modules intend to adaptively aggregate multi-level contextual information on point clouds, and make SparseDet be able to strongly enhance the information representation capability of object proxies so as to improve the performance of 3D detection with low computational costs.

A. Local Multi-scale Feature Aggregation

Most LiDAR-based sparse detection methods [33]–[36] utilize center voxel features as object proxies for detection. Although using center features as object proxies provides accurate positional information, a single center voxel-feature is insufficient to fully capture the entire information of an object. This severely weakens the expressive capability of the object proxies. Therefore, we propose LMFA module to compensate for the shortcomings. In the LMFA module, we focus on learning the local contextual information around an object, which helps to understand details such as the shape, size, and relative position of a target object. As shown in Fig. 4, we dynamically aggregate neighborhood information of key voxels through K nearest neighbor (KNN) positional relations to enhance their feature representation capability. The aggregated key voxel features will then be used to initialize the sparse object queries. It is worth noting that considering the distribution differences in 3D object scales, we extend LMFA to multiple-scale spaces. Thus, LMFA primarily consists of two steps, **Sparse Key Voxel Selection** and **Fusion Of Voxel Features From Different Scales**.

1) *Sparse Key Voxel Selection*: First, we voxelize point clouds and feed them into a 3D sparse convolutional backbone network. Referring to VoxelNeXt [35], we add two additional downsampling layers to the 3D sparse backbone network [25]. This step serves two key purposes. Firstly, it constructs multi-scale feature spaces through the additional downsampling process to facilitate the subsequent feature aggregation in LMFA module. Secondly, through the additional sampling and

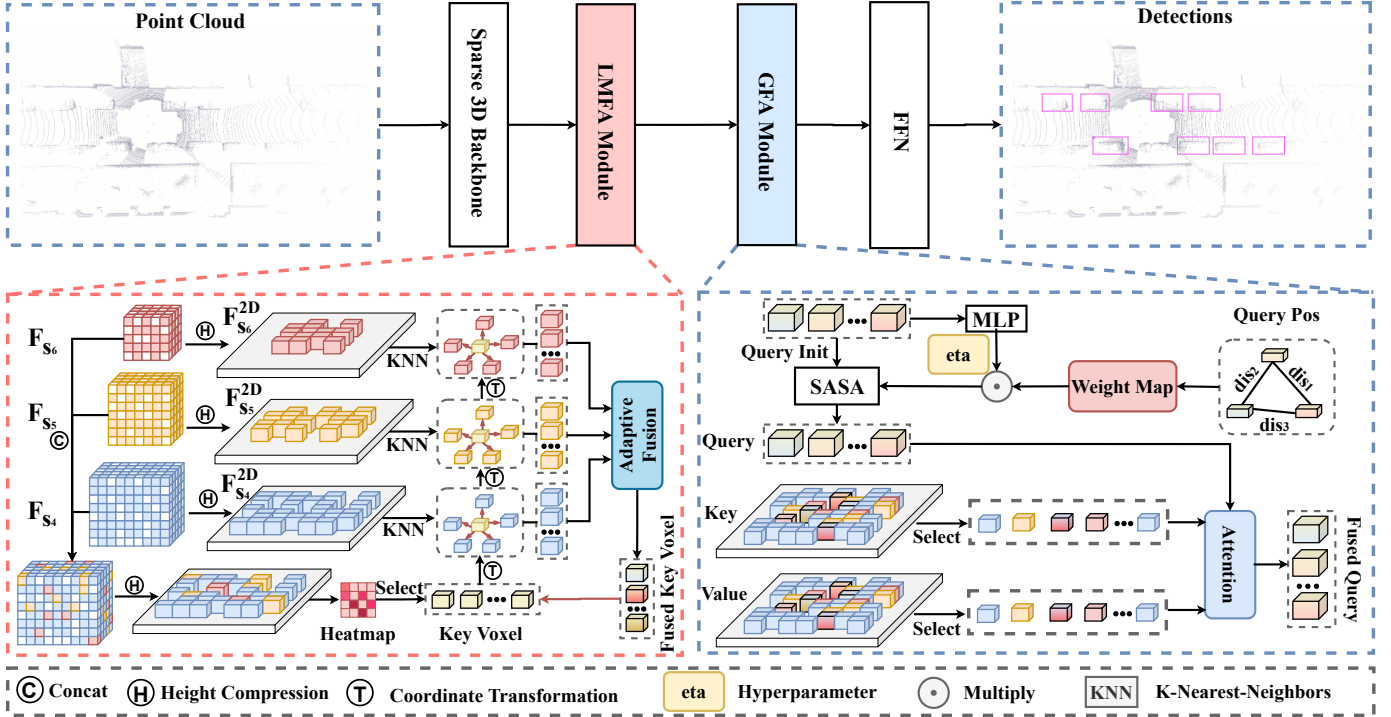


Fig. 3: The framework of our SparseDet. First, we voxelizes point clouds and feed voxels into a 3D sparse convolution backbone. Then, we perform high compression [35] on sparse voxel features ($F_{s_4}, F_{s_5}, F_{s_6}$) of the last three layers in the 3D backbone to obtain 2D sparse features of these three layers, denoted as $F_{s_4}^{2D}, F_{s_5}^{2D}$ and $F_{s_6}^{2D}$. In LMFA, we concat F_{s_4}, F_{s_5} and F_{s_6} to obtain F_{Fusion} . After applying high compression [35] on F_{Fusion} , we have F_{Fusion}^{2D} and then perform key voxel position prediction using a heatmap. Through coordinate transformation, we convert the key voxel features to the spaces of F_{s_4}, F_{s_5} and F_{s_6} and aggregate the neighborhood voxel context based on K Nearest Neighbor (KNN) relationships. Subsequently, we replace the aggregated voxel features back into F_{Fusion} based on the indices to enhance the feature representation capability of sparse features. In GFA module, we utilizes sparse voxels as queries to adaptively aggregate global sparse voxel features, where scale-adaptive weight map allows queries to autonomously learn the receptive field for aggregating information from relevant positions. At last, the aggregated queries are fed into FFN for result prediction. Adaption Fusion means the adaptive fusion of multi-scale features and FFN is a Feed Forward Neural Network.

height compression operations, we can place voxel features in object centers which are blank to construct neighborhood relations more accurately. With the above operations, the original Sparse 3D convolutional backbone transitions from $\{F_{s_1}, F_{s_2}, F_{s_3}, F_{s_4}\}$ to $\{F_{s_1}, F_{s_2}, F_{s_3}, F_{s_4}, F_{s_5}, F_{s_6}\}$ with feature strides $\{1, 2, 4, 8, 16, 32\}$, where $F_{s_i} \in R^{N_i \times C_i}$ represents the 3D sparse voxel features for each stage, s_i means the i -th stage, N_i is the number of non-empty voxels, and C_i is the number of channels. Afterward, we transform F_{s_5} and F_{s_6} to the feature space of F_{s_4} and concatenate F_{s_4}, F_{s_5} and F_{s_6} together to obtain F_{Fusion} . Then, we perform high compression on $F_{Fusion}, F_{s_4}, F_{s_5}$ and F_{s_6} to obtain $F_{Fusion}^{2D}, F_{s_4}^{2D}, F_{s_5}^{2D}$ and $F_{s_6}^{2D}$. Specifically, following the VoxelNeXt [35], we replace all the voxel features on the ground plane and sum them up at the same positions.

To select key voxels, we use heatmap operation which predict voxel scores $Score \in R^{N_{voxel} \times Cls}$ for Cl_s classes based on the sparse voxel feature F_{Fusion}^{2D} , where N_{voxel} represents the number of non-empty voxels in F_{Fusion}^{2D} . We designate the voxels closest to an object center as positive samples and utilize FocalLoss [37] for supervision. This means that voxels with higher scores have a higher probability of

belonging to the foreground. Subsequently, we apply the top- N_{key} score operation to F_{Fusion}^{2D} to obtain N_{key} key sparse voxel candidates. Here, N_{key} is set to a default value of 500.

2) *Fusion of Voxel Features From Different Scales:* In this section, we construct a K nearest neighbor graph to obtain neighborhood information for sparse candidate voxels at different scales to gain more comprehensive local contexts which address the insufficient information representation capacity of sparse features.

After sparse key voxel selection, we obtain the features of N_{key} sparse voxels, denoted as $F_{key} \in R^{N_{key} \times C}$, where C represents the number of channels. The corresponding coordinate position indices are defined as I_{key} , with a shape of $(N_{key}, 2)$, which represents the 2D position indices. We first divide the position coordinates of the N_{key} voxels in the S_4 scale, denoted as I_{s_4} , by 2 and 4, respectively, to transform them into the lower-resolution voxel spaces of $\{S_5, S_6\}$. We then save the corresponding spatial coordinate indices as I_{s_5}, I_{s_6} . Given the position coordinate information of N_{key} sparse voxels in different scale spaces, we aim to find the K nearest voxels $N_{Neighbor}^{s_i}$ for each key voxel. The value of $N_{Neighbor}^{s_i}$ is halved as the scale space changes, which can be

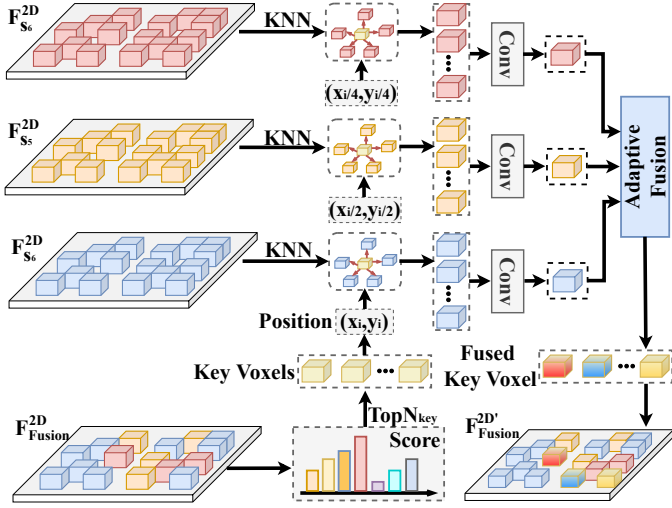


Fig. 4: The architecture details of LMFA. The LMFA module performs heatmap prediction from the F_{Fusion}^{2D} , and selects the top- N_{key} high-scoring voxels as key voxels. It then converts the position information of the key voxels to their original feature spaces according to the downsampling ratios. Based on the position information of the key voxels, LMFA module finds the KNN voxel features and fuses them by using $Conv_{1*1}$. Finally, the neighborhood features from multi-scale feature spaces are fed into the adaptive-fusion module for adaptive fusion.

determined using the following formula.

$$N_{Neighbor}^{s_i} = M/2^{i-4}, i = 4, 5, 6, \quad (1)$$

where the parameter M is set to 8 by default.

To improve the efficiency of LMFA, we employ the *KD-Tree* algorithm to obtain the indices of $N_{Neighbor}^{s_i}$ neighbors for each key voxel at a specific scale S_i , which are denoted as $I_{Neighbor}^{s_i} \in R^{N_{key} \times N_{Neighbor}^{s_i} \times 2}$. The surrounding neighbor voxel features $F_{Neighbor}^{s_i} \in R^{N_{key} \times N_{Neighbor}^{s_i} \times C}$ are obtained by indexing $F_{S_i}^{2D}$ with $I_{Neighbor}^{s_i}$. Then, MLP is utilized to aggregate the features of the neighbor voxel features $F_{Neighbor}^{s_i}$, which is performed by the following formula.

$$F_{Neighbor'}^{s_i} = MLP(F_{Neighbor}^{s_i}), \quad (2)$$

where $F_{Neighbor'}^{s_i} \in R^{N_{key} \times 1 \times C}$ represents aggregated features. By applying the aforementioned feature aggregation scheme at each feature scale in $\{S_4, S_5, S_6\}$, we can obtain aggregated features of multiple scales $F_{Neighbor} \in R^{N_{key} \times N_{scale} \times C}$, where N_{scale} is the number of scales.

Given the encoded multi-scale features of sparse voxels, a naive fusion approach is to concatenate the multi-scale features to form a single feature [44]. However, we observe that some object detections rely more on information from specific scales rather than from all scales. For instance, low-resolution feature maps lack information about small objects. Therefore, key voxels related to small objects should more effectively gather information solely from high-resolution feature maps.

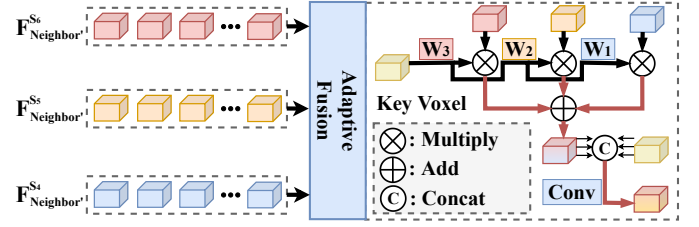


Fig. 5: The architecture of **Adaptive Fusion**, which adaptively weights and fuses neighborhood features ($F_{Neighbor'}^{S_4}$, $F_{Neighbor'}^{S_5}$ and $F_{Neighbor'}^{S_6}$) from multi-scale feature spaces for each key voxel.

We propose utilizing learnable scale weights to automatically select the scale for each key voxel F_{key} as follows.

$$W_1, W_2, W_3 = Softmax(FC(F_{key})), \quad (3)$$

$$F_{key} = Conv \left(Concat \left(F_{key}, \sum_{i=1}^{N_{scale}} W_i F_{neighbor'}^{s_i} \right) \right). \quad (4)$$

Where W_1, W_2, W_3 stand for the importance of selecting $F_{neighbor'}^{s_4}$, $F_{neighbor'}^{s_5}$, $F_{neighbor'}^{s_6}$, F_{key} is adaptively aggregated according to the scaled attention weights W_i obtained in Eq. (3). These scale weights can be learned during the training process and enable adaptive scale selection based on the characteristics of individual key voxels. Thus, we also call the step adaptive fusion.

With such a scale-selection mechanism, the scale most related to each key voxel is softly selected while the visual features from other scales are suppressed. We then place F_{key} into the F_{Fusion}^{2D} according to the position index of the F_{key} , obtaining the enhanced $F_{Fusion}^{2D'} \in R^{N_{voxels} \times C}$. The whole process of our adaptive fusion is illustrated in Fig. 5.

B. Global Feature Aggregation

The LMFA module aims to learn the local contextual information around objects by dynamically aggregating neighborhood information of key voxels through the use of nearest neighbor positional relations.

Although the fusion of neighborhood voxel features enhances the expressive power of foreground sparse voxel features, LMFA module still has limitations when dealing with sparse detection scenarios. 1) For a large object, using a single aggregated sparse voxel as a proxy for object detection still suffers from information loss since the object proxy should contain information from the entire object rather than just a local region. 2) LMFA ignores the potential collaboration between the whole scene and instance features. For example, a false negative object in a scene can be potentially rectified by enhancing its feature through interactions with instances sharing similar semantic information. Therefore, we propose the GFA (Global Feature Aggregation) module to further address the limitations of the LMFA module by learning the global structural and semantic information of the entire scene. This makes SparseDet be able to leverage the contextual

information of objects in both local and global ways to eliminate ambiguity, thereby improving the detection accuracy.

In detail, after LMFA module, we have the aggregated features of the key voxels $F_{key} \in R^{N_{key} \times C}$ and the enhanced voxel features of the entire scene $F_{Fusion}^{2D'} \in R^{N_{voxels} \times C}$, where N_{voxels} is the number of non empty voxels. Afterward, we select the top- N_{query} highest-scoring voxels based on the $Score \in R^{N_{voxels} \times Cls}$ to initialize object queries. N_{query} is set to 200 by default. We use the selected voxel positions Pos_{query} from $\mathbb{R}^{N_{query} \times 2}$ and the features F_{query} from $\mathbb{R}^{N_{query} \times C}$ to initialize the position encoding and the queries Q , as shown in Eq. (5). In this way, the initial object queries are located at or near potential object centers and contain more object information, enabling the queries to learn more efficiently and eliminating the need for multiple decoder layers to refine positions in query-based methods [53], [54].

$$\begin{aligned} Q &= F_{query} + PE_{query}, \\ PE_{query} &= MLP(MLP(Pos_{query})). \end{aligned} \quad (5)$$

Where PE_{query} means the position embedding of Pos_{query} . After obtaining the top- N_{query} queries, we use the sparse voxel features F_{Fusion}^{2D} as Key and Value in self-attention to obtain the attention score for each of top- N_{query} queries so as to perform feature aggregation. However, due to the varying number of non-empty voxels in different scenes, traditional decoders cannot be directly applied to GFA sub-module. Thus, we have conducted data analysis and found that the number of non-empty voxels in a single scene ranges approximately from 9k to 13k. We then select a fixed number of $N_{K,V}$ sparse voxel features as the Key and the Value from the sparse voxel features $F_{Fusion}^{2D'}$ based on $Score \in R^{N_{voxel} \times Cls}$. This allows SparseDet to focus more on foreground features. Here, $N_{K,V}$ is set to a default value of 10K, and any shortfall in the number of selected features is padded with zeros.

In most approaches for voxel selection [35], [53], it is common to flatten and sort $Score \in R^{N_{voxel} \times Cls}$ along the channel dimension. However, the aforementioned strategy cannot be directly applied in GFA module. The reason is that individual voxels often have similar scores for multiple classes, such as pedestrian and traffic cone. Relying solely on class scores as the selection criterion would result in the problem of repetitive feature selection. To address this issue, we propose a solution where we do not differentiate the scores for different classes. Instead, we consider the highest score within each voxel's class as the probability of that voxel being a foreground voxel. Specifically, we apply max-pooling along the channel dimension of $Score \in R^{N_{voxel} \times Cls}$ to obtain $Score' \in R^{N_{voxel} \times 1}$, which represents the highest score for each voxel regardless of its class. Next, we select $N_{K,V}$ sparse voxel features based on $Score'$ as the Key and the Value denoted as $F_K \in R^{N_{K,V} \times C}$ and $F_V \in R^{N_{K,V} \times C}$.

In order to highlight the importance of target objects while maintaining a global perspective, GFA module should interact more with the voxel features near the queries. Inspired from [55], we introduce SASA (scale-adaptive self-attention) to GFA, allowing it to learn an appropriate receptive field guided by the queries. Firstly, SASA computes the pairwise

Algorithm 1: The GFA Workflow

Input:
The height compressed sparse voxel features: $F_{Fusion}^{2D'}$
The heatmap of sparse voxels: $Score \in R^{N_{voxels} \times Cls}$
Output: The object queries: Q

```

1 def SASA( $Q, Pos_{query}$ ):
2    $Dis = Calculate\_dis(Pos_{query})$ 
3    $eta = MLP(Q)$ 
4    $attn\_mask = Dis * eta$ 
5    $Q = self\_attention(Q, attn\_mask)$ 
6   Return  $Q$ 
7 if use GFA then
8    $top\_pro = Score.argsort()[..., : N_{query}]$ 
9    $top\_pro\_cls = top\_pro // N_{voxels}$ 
10   $top\_pro\_index = top\_pro \% Cls$ 
11   $Q_{feat} = F_{Fusion}^{2D'}.features.gather($ 
12     $index = top\_pro\_index,$ 
13     $dim = -1)$ 
14   $Pos_{query} = F_{Fusion}^{2D'}.indices.gather($ 
15     $index = top\_pro\_index,$ 
16     $dim = -1)$ 
17   $Score' = Max\_pool(Score)$ 
18   $top\_kv = Score'.argsort()[..., : N_{K,V}]$ 
19   $K, V_{feat} = F_{Fusion}^{2D'}.features.gather($ 
20     $index = top\_kv,$ 
21     $dim = -1)$ 
22   $Pos_{K,V} = F_{Fusion}^{2D'}.indices.gather($ 
23     $index = top\_kv,$ 
24     $dim = -1)$ 
25   $Q = SASA(Q, Pos_{query})$ 
26   $Q = decoder(Q_{feat}, K, V_{feat}, Pos_{query}, Pos_{K,V})$ 
27  Return  $Q$ 
28 end

```

distances $Dis \in R^{N_{query} \times N_{query}}$ between all pairs of query centers Pos_{query} as below.

$$Dis_{i,j} = \sqrt{(X_{Pos}^i - X_{Pos}^j)^2 + (Y_{Pos}^i - Y_{Pos}^j)^2}, \quad (6)$$

where (X_{Pos}^i, Y_{Pos}^i) denotes the position of the i -th query. Consequently, updated queries can be obtained in the following.

$$Q = softmax\left(\frac{QK^T}{\sqrt{d}} + \eta \log(Dis)\right)V, \quad (7)$$

where η controls the receptive field of each query and is generated through a linear transformation. In this way, the queries Q can dynamically adjust the size of receptive fields and prioritize features in the vicinity of the query centers. The workflow of the GFA module is detailed in Alg. 1. Afterwards, the aggregated and refined queries Q are passed through a FFN (Feed Forward Network) layer for object prediction.

IV. EXPERIMENTS

In this section, we present the details of each dataset and the experimental setup of SparseDet, and evaluate SparseDet's

performance of 3D object detection on KITTI [41] and nuScenes [32] datasets.

A. Dataset and Evaluation Metrics

1) *KITTI dataset*: The KITTI dataset [41] provides synchronized LiDAR point clouds and front-view camera images. It consists of 7,481 training samples and 7,518 test samples. As a common practice [45], [47], [50], the training data are divided into a train set with 3712 samples and a validation set (*val* set for short) with 3,769 samples to conduct evaluation. To perform evaluation on the test dataset using the official KITTI test server, we follow the approach outlined in VoxelNext [35], use 80% of the 7,481 training samples to train our model SparseDet with the amount of 5,985 samples. The standard evaluation metric for object detection is the mean Average Precision (mAP), computed using recall at 40 positions (R40). In this work, we evaluate SparseDet and all other dense and sparse methods on the most commonly used classes including Car, Pedestrian and Cyclist using Average Precision (AP) with an Intersection over Union (IoU) threshold of 0.7, 0.5, and 0.5, respectively.

2) *nuScenes dataset*: The nuScenes dataset [32] is a large-scale 3D detection benchmark consisting of 700 training scenes, 150 validation scenes, and 150 testing scenes. The dataset was collected using six multi-view cameras and a 32-beam LiDAR sensor. It includes 360-degree object annotations for 10 object classes. To evaluate the detection performance, the primary metrics used are the mean Average Precision (mAP) and the nuScenes detection score (NDS) [32], which assesses detection accuracy in terms of classification, bounding box location, size, orientation, attributes, and velocity.

B. Implementation Details

In this section, we will provide a detailed description of the SparseDet settings for KITTI [41] and nuScenes [32]. To enable effective training on KITTI and nuScenes, we utilize 8 NVIDIA RTX 3090 24G GPUs. During inference, the batch size is set to 1 on a 3090 GPU. All latency measurements are taken on the same workstation with a 3090 GPU. We implement SparseDet based on the open-source code repositories OpenPCDet [74] and the baseline VoxelNeXt [35].

For KITTI [41], the input voxel size is set to [0.05m, 0.05m, 0.1m] and the point range is set to [0m, -40m, -3m, 70.4m, 40m, 1m] across the X, Y and Z axes, respectively. The maximum number of point clouds contained in each voxel is set to 10. During training, following the baseline [35], SparseDet is trained 80 epoches.

For nuScenes [32], the input voxel size is set to [0.075m, 0.075m, 0.2m] and the point range is set to [-54m, -54m, -5m, 54m, 54m, 3m] across the X, Y and Z axes, respectively. During training, following the baseline [35], SparseDet is trained 20 epoches. For more details concerning our method, please refer to OpenPCDet [74].

C. Comparison with State-of-the-Arts

1) *Performance on nuScenes test dataset*: We conduct experiments on larger-scale nuScenes [32] dataset using

the SOTA (state-of-the-art) fully Sparse 3D detector VoxelNeXt [35] (a typical method of the second category mentioned in related works) as the baseline to further validate the effectiveness of our SparseDet, as shown in Table I. In the table, we not only compare our SparseDet with classical sparse detectors of the first category including FSD [33] and FSDV2 [34], but also include some SOTA dense 3D detectors such as UVTR [61], Transfusion [53], LargeKernel3D [62] and PVT-SSD [63] for comparison.

Based on VoxelNeXt [35], our SparseDet achieves 66.7% mAP and 71.3% NDS, which surpasses the baseline by 2.2% mAP and 1.3% NDS. It is worth noting that our method achieves state-of-the-art AP (Average Precision) on most categories. Specifically, for the categories of “Truck”, “Barrier”, and “T.C.”, our method shows significant improvements with AP gains of 3.0%, 2.6%, and 3.5% respectively. Overall, the above results fully demonstrates the generalization and effectiveness of our method. Thanks to our LMFA and GFA modules, SparseDet is able to obtain richer and more accurate object representations by comprehensively aggregating local point cloud details and global contextual information, while also facilitating the collaboration between the entire scene and instance features. As a result, it achieves significant performance improvements across a wide range of object categories.

2) *Performance on nuScenes val dataset*: To demonstrate the effectiveness of our SparseDet, we conduct experiments on nuScenes validation dataset using VoxelNeXt [35] as the baseline. As shown in Table II, our method outperforms VoxelNeXt by 6.4%, 6.7%, and 7.3% on “C.V.”, “Motor”, and “Bike” categories in the nuScenes full validation dataset, respectively. The results demonstrate that the effective aggregation of point cloud contextual information significantly enhances the representational capacity of the sparse object detection proxies. Additionally, by designing sparse queries as object detection proxies, we avoid the issue of missing central features, as mentioned in SAFDNet [36]. The aforementioned results demonstrate the effectiveness of SparseDet in detecting both small and large objects.

3) *Performance on KITTI test set*: As shown in Table III, we compare SparseDet with the SOTA methods on KITTI test set. We note that our SparseDet shows outstanding performance at three difficulty levels of 3D and BEV detection (90.79%, 81.17%, 78.11% in 3D APs and 94.48%, 89.68%, 87.53% in BEV APs). It is worth noting that VoxelNeXt [35] have not provided the results of KITTI dataset. For fair comparison, we reproduce VoxelNeXt [35] as the baseline, following the configuration exactly as described in the original paper [35]. By Table III, Our SparseDet surpasses VoxelNeXt [45] on most metrics. Especially, on the challenging hard level tasks, we improve 1.12%, 2.72% and 2.98% in car, pedestrian, and cyclist categories, respectively. Compared to the latest dense approach, PVT-SSD [63], our method achieves superior performance, reaching 76.81% and 63.46% on the difficult levels for the car and two-wheeler categories, respectively. Overall, our SparseDet performs well on KITTI [41] test set, especially on the hard level which mostly consists of distant and small objects, strongly demonstrating the effectiveness of

TABLE I: Comparison with the SOTA methods on nuScenes test set. ‘‘C.V.’’, ‘‘Motor.’’, ‘‘Ped.’’, and ‘‘T.C.’’ are short for construction vehicle, motorcycle, pedestrian, and traffic cone, respectively.

Method		mAP	NDS	Car	Truck	C.V.	Bus	Trailer	Barrier	Motor.	Bike	Ped.	T.C.
Dense	PointPillars [24]	30.5	45.3	68.4	23.0	4.1	28.2	23.4	38.9	27.4	1.1	59.7	30.8
	3DSSD [56]	42.7	56.4	81.2	47.2	12.6	61.4	30.5	47.9	36.0	8.6	70.2	31.1
	SASA [57]	45.0	61.0	76.8	45.0	16.1	66.2	36.5	53.6	39.6	16.9	69.1	29.9
	CenterPoint [37]	58.0	65.5	84.6	51.0	17.5	60.2	53.2	70.9	53.7	28.7	83.4	76.7
	HotSpotNet [58]	59.3	66.0	83.1	50.9	23.0	56.4	53.3	71.6	63.5	36.6	81.3	73.0
	InfoFocus [59]	39.5	39.5	77.9	31.4	10.7	44.8	37.3	47.8	29.0	6.1	63.4	46.5
	AFDetV2 [49]	62.4	68.5	86.3	54.2	26.7	62.5	58.9	71.0	63.8	34.3	85.8	80.1
	VISTA [60]	63.0	69.8	84.4	55.1	25.1	63.7	54.2	71.4	70.0	45.4	82.8	78.5
	Focals Conv [50]	63.8	70.0	86.7	56.3	23.8	67.7	59.5	74.1	64.5	36.3	81.4	81.4
	TransFusion-L [53]	65.5	70.2	86.2	56.7	28.2	66.3	58.8	78.2	68.3	44.2	86.1	82.0
	UVTR [61]	67.1	71.1	87.5	56.0	33.8	67.5	59.5	73.0	73.4	54.8	86.3	79.6
	LargeKernel3D [62]	65.3	70.5	85.9	55.3	26.8	65.7	62.1	75.5	72.5	46.6	85.6	80.0
	PVT-SSD [63]	53.6	65.0	79.4	43.8	21.7	62.1	34.2	67.1	53.4	38.2	79.8	56.6
	Sparse	FSD [33]	62.5	68.7	-	-	-	-	-	-	-	-	-
FSDV2 [34]		66.2	71.7	83.7	51.6	32.5	66.4	59.1	78.7	71.4	51.7	87.1	80.3
VoxelNeXt [35]		64.5	70.0	84.6	53.0	28.7	64.7	55.8	74.6	73.2	45.7	85.8	79.0
	SparseDet	66.7+2.2	71.9+1.9	86.2+1.6	56.0+3.0	30.2+1.5	66.5+1.8	58.4+2.6	78.7+4.1	73.7+0.5	46.8+1.1	87.5+1.7	82.5+3.5

TABLE II: Comparison with the baseline on nuScenes *val* dataset. ‘C.V.’, ‘Ped.’, and ‘T.C.’ are short for construction vehicle, pedestrian, and traffic cone, respectively.

Dataset Split	Method	mAP	NDS	Car	Truck	C.V.	Bus	Trailer	Barrier	Motor.	Bike	Ped.	T.C.
full	VoxelNeXt*	60.8	68.1	83.8	57.7	20.8	71.5	38.6	67.6	63.0	51.5	84.5	69.0
	SparseDet	65.3+4.5	70.3+2.2	87.5+3.7	60.2+2.5	27.2+6.4	75.8+4.3	40.4+1.8	73.1+5.5	69.7+6.7	58.8+7.3	86.5+2.0	63.4+4.4
$\frac{1}{4}$	VoxelNeXt*	51.8	60.7	80.2	48.1	15.4	63.1	26.1	59.3	52.5	35.5	81.6	56.2
	SparseDet	55.3+3.5	62.7+2.0	82.7+2.5	51.8+3.7	18.8+3.4	64.3+1.2	27.6+1.5	64.6+5.3	60.1+7.6	39.1+3.6	81.6	62.7+6.5
$\frac{1}{8}$	VoxelNeXt*	46.6	55.4	78.0	41.8	15.9	57.7	20.6	53.1	49.4	23.7	76.3	49.4
	SparseDet	49.5+2.9	58.2+2.8	81.3+3.3	44.8+3.0	17.4+1.5	63.2+5.5	24.1+3.5	54.2+1.1	54.2+4.8	25.7+2.0	78.8+2.5	52.6+3.2

* denotes re-implement result.

The color red indicates improvement.

TABLE III: Performance comparison with SOTA methods on KITTI test set for 3D detection with an average precision of 40 sampling recall points evaluated on KITTI server. ‘L’ represents LiDAR.

Method	Car						Pedestrian						Cyclist						
	AP_{3D} (%)			AP_{BEV} (%)			AP_{3D} (%)			AP_{BEV} (%)			AP_{3D} (%)			AP_{BEV} (%)			
	Easy	Mod	Hard	Easy	Mod	Hard	Easy	Mod	Hard	Easy	Mod	Hard	Easy	Mod	Hard	Easy	Mod	Hard	
Dense	BSAODet [64]	88.89	81.74	77.14	-	-	51.71	43.63	41.09	-	-	-	82.65	67.79	60.26	-	-	-	
	H ² 3D R-CNN [65]	90.43	81.55	77.22	92.85	88.87	86.07	52.75	45.26	41.56	58.14	50.43	46.72	78.67	62.74	55.78	82.76	67.90	60.49
	SECOND [25]	84.65	75.96	68.71	91.81	86.37	81.04	-	-	-	-	-	-	-	-	-	-	-	-
	PointPillars [24]	82.58	74.31	68.99	90.07	86.56	82.81	51.45	41.92	38.89	57.60	48.64	45.78	77.10	58.65	51.92	79.90	62.73	55.58
	SIEV-Net [66]	85.21	76.18	70.60	-	-	-	54.00	44.80	41.11	-	-	-	78.75	59.99	52.37	-	-	-
	VoxSet [67]	88.53	82.06	77.46	-	-	-	-	-	-	-	-	-	-	-	-	-	-	-
	TANet [68]	83.81	75.38	67.66	-	-	-	54.92	46.67	42.42	-	-	-	73.84	59.86	53.46	-	-	-
	Part-A ² [48]	87.81	78.49	73.51	91.70	87.79	84.61	53.10	43.35	40.06	59.04	49.81	45.92	79.17	63.52	56.93	83.43	68.73	61.85
	Voxel RCNN [45]	90.90	81.62	77.06	-	-	-	-	-	-	-	-	-	-	-	-	-	-	-
	Voxel RCNN *	90.76	81.69	77.42	92.89	89.97	84.69	52.57	44.86	39.09	57.66	49.32	44.15	77.54	64.00	53.15	79.68	67.56	62.70
	PV-RCNN [47]	90.25	81.43	76.82	94.98	90.65	86.14	52.17	43.29	59.86	50.57	46.74	78.60	63.71	57.65	82.49	68.89	62.41	
	PV-RCNN *	90.61	81.51	76.81	94.68	90.87	86.19	52.10	43.63	40.44	60.06	50.43	46.81	78.58	63.83	57.71	82.50	68.93	62.57
	PV-RCNN++ * [69]	87.72	81.29	76.78	91.93	89.75	85.77	47.50	40.31	38.15	51.20	44.61	42.55	80.34	67.46	60.38	83.83	71.51	64.77
	PVT-SSD [63]	90.65	82.29	76.85	95.23	91.63	86.43	-	-	-	-	-	-	-	-	-	-	-	-
Sparse	VoxelNeXt * [35]	89.10	80.35	76.99	93.03	89.49	86.40	52.10	42.72	39.08	57.19	48.27	44.55	81.33	65.31	57.43	83.34	67.55	59.61
	SparseDet	90.79	81.17	78.11	94.48	89.68	87.53	52.92	44.61	41.80	59.84	50.75	44.57	81.93	65.95	60.41	83.16	69.04	63.46

* denotes re-implement result.

our method.

4) *Performance on KITTI val dataset*: We further provide the results of the KITTI validation set to better present the detection performance of our SparseDet, as shown in Table IV. There are significant improvements compared to the baseline VoxelNeXt [35] on moderate and hard levels. Meanwhile, compared to dense detection approaches, our method also demonstrates competitive performance. For sparse detectors [35] that treat a single center feature as a physical detection proxy, insufficient aggregation contextual information weakens the ability to present objects at central points, thus limiting the performance of the detection methods. The key factor that

makes SparseDet effective is its ability to comprehensively aggregate contextual information at critical locations, thereby enhancing the object proxies’ capacity to present objects.

5) *Comparison with Other Sparse Detectors*: To demonstrate the effectiveness of our SparseDet, we conduct a comparative evaluation on nuScenes [32] dataset by comparing SparseDet against other sparse detection frameworks [33]–[35] as shown in Table V. In the table, we also compare the inference speed, the size of parameters and memory usage of SparseDet with prior sparse detection frameworks besides accuracy measurements. SparseDet achieves the highest mAP, meanwhile maintains an excellent inference speed. Compared

TABLE IV: Performance comparison with the SOTA methods on KITTI *val* dataset for car class. The results are reported by the mAP with 0.7 IoU threshold and 40 recall points. ‘L’ represents LiDAR.

Method	AP_{3D} (%)			AP_{BEV} (%)		
	Easy	Mod.	Hard	Easy	Mod.	Hard
PointRCNN [28]	88.88	78.63	77.38	-	-	-
H ² 3D R-CNN [65]	89.63	85.20	79.08	-	-	-
SECOND [25]	87.43	76.48	69.10	-	-	-
MedTr-TSD [70]	89.27	84.24	78.85	-	-	-
CT3D [71]	92.85	85.82	83.46	96.14	91.88	89.63
Part-A ² [48]	89.47	79.47	78.54	90.42	88.61	87.31
Voxel RCNN [45]	92.38	85.29	82.86	95.52	91.25	88.99
PV-RCNN [47]	92.57	84.83	82.69	95.76	91.11	88.93
PC-RGNN [72]	90.94	81.43	80.45	-	-	-
PDV [73]	92.56	85.29	83.05	-	-	-
SIENet [66]	91.96	84.45	82.64	-	-	-
VoxelNeXt* [35]	92.51	84.35	82.71	95.24	90.28	90.45
SparseDet	93.81	84.78	84.33	95.30	92.55	91.02

* denotes re-implement result.

TABLE V: Runtime comparison on nuScenes [32] dataset. Mem. denotes the training GPU memory measured following [25]. FPS (frame per second) is the inference speed measured on a single NVIDIA 3090 GPU with a batch size of 1.

Method	mAP	NDS	FPS	#Params	Mem.(G)
FSD [33]	62.5	68.7	10.1	11.7M	4.97
FSDV2 [34]	66.2	71.7	10.3	10.6M	4.80
VoxelNeXt [35]	64.5	70.0	15.1	7.62M	3.42
SparseDet	66.7	71.9	13.5	7.98M	3.71

to the baseline VoxelNeXt, SparseDet achieves a 2.2% increase in mAP performance, but only has an increase of 0.36M parameters. Additionally, SparseDet does not need any auxiliary task. This is the main reason that SparseDet outperforms previous FSD [33] and FSDV2 [34] methods in inference speed, the size of parameters, and training memory consumption.

D. Ablation Study

1) *Effect of LMFA and GFA modules* : This section discusses the results of ablation experiments conducted on the baseline detector VoxelNeXt [35] to evaluate the performance of each component in SparseDet. The results are reported in Table VI and Table VII for KITTI and nuScenes $\frac{1}{4}$ subset, respectively. Table VI shows the initial AP scores for both AP_{3D} and AP_{BEV} on KITTI, which are 78.44% and 87.10%, respectively. As shown in Table VI, LMFA and GFA modules lead to a significant improvement in performance on the hard-level KITTI tasks, with an increase of 4.27% and 3.35% for AP_{3D} and AP_{BEV} , respectively. All the improvements do not significantly increase the model’s parameter or weaken the inference speed.

As shown in Table VII, when using LMFA module, SparseDet achieves an excellent performance improvement, which indicates that effectively aggregating contextual information can better enhance the representation ability of sparse features, thereby improving the performance of the sparse 3D object detector. Compared to LMFA module, which focuses

TABLE VI: Effect of each component in our SparseDet. Results are reported on KITTI *val* set for car category with VoxelNeXt. FPS (frame per second) is the inference speed measured on a single NVIDIA 3090 GPU with a batch size of 1.

LMFA	GFA	Hard		#Params	FPS
		AP_{3D} (%)	AP_{BEV} (%)		
		78.44	87.10	7.45 M	20.1
✓		81.67+3.23	89.24+2.14	7.55 M	18.6
✓	✓	84.33+2.66	91.02+1.78	7.79 M	17.9

The color red indicates improvement.

TABLE VII: Effect of each component in our SparseDet. Results are reported on nuScenes *val* set (trained on $\frac{1}{4}$ subset) with VoxelNeXt. FPS (frame per second) is the inference speed measured on a single NVIDIA 3090 GPU with a batch size of 1.

LMFA	GFA	mAP	NDS	#Params	FPS
		51.8	60.7	7.62M	15.1
✓		52.9+1.1	61.4+0.7	7.71M	14.0
✓	✓	55.3+2.4	62.7+1.3	7.98M	13.5

The color red indicates improvement.

on learning local details of point clouds, the GFA module dynamically learns information from global sparse features. This promotes collaboration between scene and instance features, resulting in richer and more accurate object representations. When LMFA and GFA are integrated, this enhancement effect is further amplified, leading to improvements of 2.4% in mAP and 1.3% in NDS. In summary, our ablation experiments show that SparseDet effectively enhances the performance of the baseline on challenging datasets. The research results underscore the importance of contextual information aggregation in sparse detection frameworks and provide valuable insights for designing effective aggregation strategies.

2) *Effect of the number of M* : The selection of neighboring voxel features, to enhance the feature representation at key locations, is a critical component of LMFA module. In this section, we will discuss the choice of the number of neighboring voxels M , and its corresponding effectiveness. Therefore, we configure different values for the hyperparameter M (the number of neighboring voxels) including 4, 8, 16, and 32. As shown in Table VIII, the variation in the value of M does not exhibit significant impact on the model’s performance. It is worth noting that when M is set to 8, our SparseDet model achieves the highest mAP, while setting M to 16 results in the best NDS performance. Considering the overall model performance, inference time, training memory, and model parameters, we ultimately set M to 8 as the default value.

3) *Effect of the number of N_{key}* : As shown in Table IX, we conduct an ablation study on the number of key voxels N_{key} within LMFA module on the nuScenes validation dataset. We configure the value of the hyperparameter N_{key} among 500, 1000, 1500, and 2000. In summary, as the value of N_{key} increases, the performance of the SparseDet correspondingly

TABLE VIII: Effect of the number of M on nuScenes *val* set (trained on $\frac{1}{4}$ subset) with SparseDet.

M	mAP	NDS	FPS	#params	Mem.(G)
4	54.7	62.5	13.8	7.92M	3.60
8	55.3	62.7	13.5	7.98M	3.71
16	55.2	62.9	12.9	8.11M	3.88
32	54.3	62.1	12.1	8.37M	4.01

TABLE IX: Effect of the number of N_{key} on nuScenes *val* set (trained on $\frac{1}{4}$ subset) with SparseDet.

N_{key}	mAP	NDS	FPS	#params	Mem.(G)
500	55.3	62.7	13.5	7.98M	3.71
1000	55.6	63.2	12.9	7.98M	3.89
1500	55.6	62.6	12.0	7.98M	3.93
2000	55.8	63.0	11.6	7.98M	3.98

achieves varying degrees of improvements. Another observation from the Table is that the model’s performance does not exhibit a strong sensitivity to the changes of N_{key} . Although simply increasing the value of N_{key} can enhance the model’s performance, it comes at the cost of reduced inference speed. After weighing the model’s accuracy and inference latency, we ultimately select 500 as the default value for N_{key} .

4) *Effect of the number of $N_{K,V}$* : As shown in Table X, we conduct an ablation study on the hyperparameter $N_{K,V}$ in the GFA module on the nuScenes validation set. We configure the value of the hyperparameter $N_{K,V}$ among 6000, 8000, 10000, and 12000. It is worth noting that when the value of $N_{K,V}$ is set to 12000, SparseDet achieves the highest mAP and NDS scores, but it exhibits the lowest inference speed. After weighing the model’s accuracy and inference latency, we ultimately set $N_{K,V}$ to 10000 as the default value.

5) *The performance of model in different distances*: Compared to dense detectors, a key advantage of sparse detectors is their ability to extend the models’ long-range detection capabilities without a significant increase in inference latency. Consequently, the stable detection of distant targets is a critical metric for evaluating the performance of sparse detectors. To better understand the superior performance of our SparseDet at long distances, we provide performance metrics for different distance ranges in Table XI and Table XII. Specifically, compared to the VoxelNeXt [35], our metrics show a more significant improvement, especially in the distance ranges of 20-40m and 40m-inf. For example, in 3D detection at 40m-inf of KITTI, our SparseDet improves AP_{3D} by 9.28%. In BEV detection at 40m-inf, our SparseDet improved AP_{BEV} by 9.40%. And on nuScenes dataset, in the detection at 40m inf, our SparseDet improves by 4.1% and 3.6% on mAP and NDS, respectively. These results clearly reflect the advantages of our SparseDet model in longer-range detection.

E. Visualization

In Fig. 6, compared to VoxelNeXt, we illustrate the superiority of our SparseDet for long-range/remote object detection,

TABLE X: Effect of the number of $N_{K,V}$ on nuScenes *val* set (trained on $\frac{1}{4}$ subset) with SparseDet.

$N_{K,V}$	mAP	NDS	FPS	#params	Mem.(G)
6000	54.1	61.7	14.2	7.98M	3.51
8000	54.9	62.3	13.8	7.98M	3.62
10000	55.3	62.7	13.5	7.98M	3.71
12000	55.4	62.9	13.0	7.98M	3.83

TABLE XI: Performance of different distances. The results are evaluated with AP calculated by 40 recall positions and 0.7 IoU threshold for car category in the **hard** level on KITTI *val* set.

Method	$AP_{3D}(\%)$			$AP_{BEV}(\%)$		
	0-20m	20-40m	40m-inf	0-20m	20-40m	40m-inf
VoxelNeXt*	94.70	77.81	35.49	95.25	87.27	54.23
SparseDet	95.72+1.02	79.95+2.14	44.77+9.28	96.66+1.41	89.26+1.99	63.63+9.40

* denotes re-implement result.

The color **red** indicates improvement to our SparseDet.

TABLE XII: Performance of different distances. The results are evaluated with mAP and NDS on nuScenes *val* set.

Method	mAP(%)			NDS(%)		
	0-20m	20-40m	40m-inf	0-20m	20-40m	40m-inf
VoxelNeXt*	75.9	49.5	22.3	76.3	60.2	42.2
SparseDet	77.6+1.7	55.3+5.8	26.4+4.1	77.3+1.0	63.8+3.6	45.6+3.6

* denotes re-implement result.

The color **red** indicates improvement to our SparseDet.

using the detection range of 0-70.4m for car category in KITTI as a case. According to the figure, our SparseDet has a false positive result, but there is no missed instance. Whereas, VoxelNeXt [35] suffers from the missing of remote objects. This can be attributed to the fact that Our SparseDet fully utilizes the multi-scale contextual semantic information in point clouds, which are crucial for remote objects in sparse point clouds since these objects more obviously suffer from the

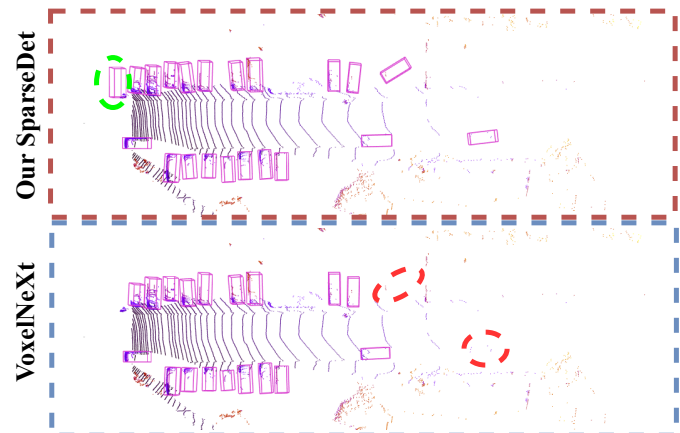


Fig. 6: Visualization comparison between VoxelNeXt and our SparseDet in long-range detection, where false positives and false negatives are highlighted in **green** and **red**, respectively.

lack of information. Overall, our method exhibits a significant improvement in the precision of remote object detection.

V. CONCLUSIONS

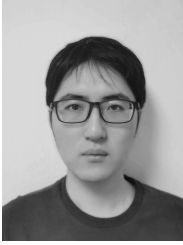
In this work, we propose SparseDet, a simple and effective framework for fully sparse 3D object detection. Specifically, based on VoxelNeXt, we have designed an efficient sparse detection framework that more reasonably utilizes instance-level and scene-level point cloud contextual information. This has significantly enhanced the expression capability of object proxies, thereby substantially improving the detection performance of a sparse detector. Comprehensive experimental results demonstrate that SparseDet significantly improves the performance compared with the baseline on the KITTI and nuScenes datasets. We hope our work can provide new insights into sparse detectors for autonomous driving.

Currently, the research works on sparse 3D detectors are not sufficient as the other directions such as multi-modal 3D detection. This makes the comparison methods of 3D sparse frameworks be limited. However, for real-world applications, the latency of a model is very important. Therefore, research on fully sparse and fast detectors deserves more attention and focus.

REFERENCES

- [1] L. Wang, X. Zhang, Z. Song, J. Bi, G. Zhang, H. Wei, L. Tang, L. Yang, J. Li, C. Jia *et al.*, “Multi-modal 3d object detection in autonomous driving: A survey and taxonomy,” *IEEE Transactions on Intelligent Vehicles*, 2023.
- [2] Z. Song, L. Liu, F. Jia, Y. Luo, G. Zhang, L. Yang, L. Wang, and C. Jia, “Robustness-aware 3d object detection in autonomous driving: A review and outlook,” *arXiv preprint arXiv:2401.06542*, 2024.
- [3] Z. Song, H. Wei, L. Bai, L. Yang, and C. Jia, “GraphAlign: Enhancing Accurate Feature Alignment by Graph matching for Multi-Modal 3D Object Detection,” in *Proceedings of the IEEE/CVF International Conference on Computer Vision (ICCV)*, October 2023, pp. 3358–3369.
- [4] Z. Song, C. Jia, L. Yang, H. Wei, and L. Liu, “GraphAlign++: An Accurate Feature Alignment by Graph Matching for Multi-Modal 3D Object Detection,” *IEEE Transactions on Circuits and Systems for Video Technology*, pp. 1–1, 2023.
- [5] S. Xu, F. Li, Z. Song, J. Fang, S. Wang, and Z.-X. Yang, “Multi-sem fusion: multimodal semantic fusion for 3d object detection,” *IEEE Transactions on Geoscience and Remote Sensing*, 2024.
- [6] J. Bi, H. Wei, G. Zhang, K. Yang, and Z. Song, “Dyfusion: Cross-attention 3d object detection with dynamic fusion,” *IEEE Latin America Transactions*, vol. 22, no. 2, pp. 106–112, 2024.
- [7] G. Zhang, J. Xie, L. Liu, Z. Wang, K. Yang, and Z. Song, “Urformer: Unified representation lidar-camera 3d object detection with transformer,” in *Chinese Conference on Pattern Recognition and Computer Vision (PRCV)*. Springer, 2023, pp. 401–413.
- [8] X. Zhang, L. Wang, G. Zhang, T. Lan, H. Zhang, L. Zhao, J. Li, L. Zhu, and H. Liu, “Ri-fusion: 3d object detection using enhanced point features with range-image fusion for autonomous driving,” *IEEE Transactions on Instrumentation and Measurement*, vol. 72, pp. 1–13, 2022.
- [9] Z. Song, G. Zhang, L. Liu, L. Yang, S. Xu, C. Jia, F. Jia, and L. Wang, “Robofusion: Towards robust multi-modal 3d object detection via sam,” *arXiv preprint arXiv:2401.03907*, 2024.
- [10] L. Wang, X. Zhang, B. Xv, J. Zhang, R. Fu, X. Wang, L. Zhu, H. Ren, P. Lu, J. Li *et al.*, “Interfusion: Interaction-based 4d radar and lidar fusion for 3d object detection,” in *2022 IEEE/RSJ International Conference on Intelligent Robots and Systems (IROS)*. IEEE, 2022, pp. 12 247–12 253.
- [11] Z. Song, L. Yang, S. Xu, L. Liu, D. Xu, C. Jia, F. Jia, and L. Wang, “Graphbev: Towards robust bev feature alignment for multi-modal 3d object detection,” *arXiv preprint arXiv:2403.11848*, 2024.
- [12] Z. Song, G. Zhang, J. Xie, L. Liu, C. Jia, S. Xu, and Z. Wang, “Voxelnextfusion: A simple, unified and effective voxel fusion framework for multi-modal 3d object detection,” *arXiv preprint arXiv:2401.02702*, 2024.
- [13] B. Xu, X. Zhang, L. Wang, X. Hu, Z. Li, S. Pan, J. Li, and Y. Deng, “Rpf-net: A 4d radar pillar feature attention network for 3d object detection,” in *2021 IEEE International Intelligent Transportation Systems Conference (ITSC)*. IEEE, 2021, pp. 3061–3066.
- [14] L. Wang, X. Zhang, J. Li, B. Xv, R. Fu, H. Chen, L. Yang, D. Jin, and L. Zhao, “Multi-modal and multi-scale fusion 3d object detection of 4d radar and lidar for autonomous driving,” *IEEE Transactions on Vehicular Technology*, 2022.
- [15] P. Wang, L. Shi, B. Chen, Z. Hu, J. Qiao, and Q. Dong, “Pursuing 3-D scene structures with optical satellite images from affine reconstruction to Euclidean reconstruction,” *IEEE Transactions on Geoscience and Remote Sensing*, vol. 60, pp. 1–14, 2022.
- [16] Y. Li, Z. Ge, G. Yu, J. Yang, Z. Wang, Y. Shi, J. Sun, and Z. Li, “Bevdepth: Acquisition of reliable depth for multi-view 3d object detection,” in *Proceedings of the AAAI Conference on Artificial Intelligence*, vol. 37, no. 2, 2023, pp. 1477–1485.
- [17] L. Yang, K. Yu, T. Tang, J. Li, K. Yuan, L. Wang, X. Zhang, and P. Chen, “Bevheight: A robust framework for vision-based roadside 3d object detection,” in *Proceedings of the IEEE/CVF Conference on Computer Vision and Pattern Recognition*, 2023, pp. 21 611–21 620.
- [18] L. Yang, T. Tang, J. Li, P. Chen, K. Yuan, L. Wang, Y. Huang, X. Zhang, and K. Yu, “Bevheight++: Toward robust visual centric 3d object detection,” *arXiv preprint arXiv:2309.16179*, 2023.
- [19] J. Huang and G. Huang, “Bevdet4d: Exploit temporal cues in multi-camera 3d object detection,” *arXiv preprint arXiv:2203.17054*, 2022.
- [20] L. Yang, X. Zhang, J. Li, L. Wang, M. Zhu, C. Zhang, and H. Liu, “Mix-teaching: A simple, unified and effective semi-supervised learning framework for monocular 3d object detection,” *IEEE Transactions on Circuits and Systems for Video Technology*, 2023.
- [21] Z. Song, L. Liu, F. Jia, Y. Luo, G. Zhang, L. Yang, L. Wang, and C. Jia, “Robustness-aware 3d object detection in autonomous driving: A review and outlook,” *arXiv preprint arXiv:2401.06542*, 2024.
- [22] L. Wang, X. Zhang, Z. Song, J. Bi, G. Zhang, H. Wei, L. Tang, L. Yang, J. Li, C. Jia *et al.*, “Multi-modal 3D Object Detection in Autonomous Driving: A Survey and Taxonomy,” *IEEE Transactions on Intelligent Vehicles*, 2023.
- [23] L. Wang, X. Zhang, Z. Song, J. Bi, G. Zhang, H. Wei, L. Tang, L. Yang, J. Li, C. Jia, and L. Zhao, “Multi-Modal 3D Object Detection in Autonomous Driving: A Survey and Taxonomy,” *IEEE Transactions on Intelligent Vehicles*, vol. 8, no. 7, pp. 3781–3798, 2023.
- [24] A. H. Lang, S. Vora, H. Caesar, L. Zhou, J. Yang, and O. Beijbom, “PointPillars: Fast Encoders for Object Detection from Point Clouds.” *CoRR*, vol. abs/1812.05784, 2018. [Online]. Available: <http://dblp.uni-trier.de/db/journals/corr/corr1812.html#abs-1812-05784>
- [25] Y. Yan, Y. Mao, and B. Li, “SECOND: Sparsely Embedded Convolutional Detection.” *Sensors*, vol. 18, no. 10, p. 3337, 2018. [Online]. Available: <http://dblp.uni-trier.de/db/journals/sensors/sensors18.html#YanML18>
- [26] Y. Zhou and O. Tuzel, “VoxelNet: End-to-End Learning for Point Cloud Based 3D Object Detection.” in *CVPR*. IEEE Computer Society, 2018, pp. 4490–4499. [Online]. Available: <http://dblp.uni-trier.de/db/conf/cvpr/cvpr2018.html#ZhouT18>
- [27] W. Shi and R. Rajkumar, “Point-gnn: Graph neural network for 3d object detection in a point cloud,” in *Proceedings of the IEEE/CVF conference on computer vision and pattern recognition*, 2020, pp. 1711–1719.
- [28] S. Shi, X. Wang, and H. Li, “PointRCNN: 3D Object Proposal Generation and Detection From Point Cloud.” in *CVPR*. Computer Vision Foundation / IEEE, 2019, pp. 770–779. [Online]. Available: <http://dblp.uni-trier.de/db/conf/cvpr/cvpr2019.html#ShiWL19>
- [29] Z. Song, H. Wei, C. Jia, Y. Xia, X. Li, and C. Zhang, “VP-Net: Voxels as Points for 3D Object Detection,” *IEEE Transactions on Geoscience and Remote Sensing*, 2023.
- [30] L. Wang, Z. Song, X. Zhang, C. Wang, G. Zhang, L. Zhu, J. Li, and H. Liu, “SAT-GCN: Self-attention graph convolutional network-based 3D object detection for autonomous driving,” *Knowledge-Based Systems*, vol. 259, p. 110080, 2023.
- [31] L. Wang, X. Zhang, F. Zhao, C. Wu, Y. Wang, Z. Song, L. Yang, B. Xu, J. Li, and S. S. Ge, “Fuzzy-nms: Improving 3d object detection with fuzzy classification in nms,” *IEEE Transactions on Intelligent Vehicles*, 2024.
- [32] H. Caesar, V. Bankiti, A. H. Lang, S. Vora, V. E. Liong, Q. Xu, A. Krishnan, Y. Pan, G. Baldan, and O. Beijbom, “nusenes: A multimodal dataset for autonomous driving,” in *Proceedings of the IEEE/CVF conference on computer vision and pattern recognition*, 2020, pp. 11 621–11 631.

- [33] L. Fan, F. Wang, N. Wang, and Z.-X. Zhang, "Fully sparse 3d object detection," *Advances in Neural Information Processing Systems*, vol. 35, pp. 351–363, 2022.
- [34] L. Fan, F. Wang, N. Wang, and Z. Zhang, "Fsd v2: Improving fully sparse 3d object detection with virtual voxels," *arXiv preprint arXiv:2308.03755*, 2023.
- [35] Y. Chen, J. Liu, X. Zhang, X. Qi, and J. Jia, "Voxelnext: Fully sparse voxelnet for 3d object detection and tracking," in *Proceedings of the IEEE/CVF Conference on Computer Vision and Pattern Recognition*, 2023, pp. 21 674–21 683.
- [36] G. Zhang, J. Chen, G. Gao, J. Li, S. Liu, and X. Hu, "Safednet: A simple and effective network for fully sparse 3d object detection."
- [37] T. Yin, X. Zhou, and P. Krahenbuhl, "Center-based 3d object detection and tracking," in *Proceedings of the IEEE/CVF conference on computer vision and pattern recognition*, 2021, pp. 11 784–11 793.
- [38] G. Zhang, J. Chen, G. Gao, J. Li, and X. Hu, "Hednet: A hierarchical encoder-decoder network for 3d object detection in point clouds."
- [39] H. Wu, J. Deng, C. Wen, X. Li, C. Wang, and J. Li, "CasA: A cascade attention network for 3-D object detection from LiDAR point clouds," *IEEE Transactions on Geoscience and Remote Sensing*, vol. 60, pp. 1–11, 2022.
- [40] T. Wang, Z. Xinge, J. Pang, and D. Lin, "Probabilistic and geometric depth: Detecting objects in perspective," in *Conference on Robot Learning*. PMLR, 2022, pp. 1475–1485.
- [41] A. Geiger, P. Lenz, and R. Urtasun, "Are we ready for autonomous driving? the kitti vision benchmark suite," in *Computer Vision and Pattern Recognition (CVPR), 2012 IEEE Conference on*. IEEE, 2012, pp. 3354–3361. [Online]. Available: <https://ieeexplore.ieee.org/abstract/document/6248074>
- [42] P. Sun, H. Kretschmar, X. Dotiwalla, A. Chouard, V. Patnaik, P. Tsui, J. Guo, Y. Zhou, Y. Chai, B. Caine *et al.*, "Scalability in perception for autonomous driving: Waymo open dataset," in *Proceedings of the IEEE/CVF conference on computer vision and pattern recognition*, 2020, pp. 2446–2454.
- [43] X. Zhang, L. Wang, J. Chen, C. Fang, L. Yang, Z. Song, G. Yang, Y. Wang, X. Zhang, and J. Li, "Dual radar: A multi-modal dataset with dual 4d radar for autonomous driving," *arXiv preprint arXiv:2310.07602*, 2023.
- [44] H. Kuang, B. Wang, J. An, M. Zhang, and Z. Zhang, "Voxel-FPN: Multi-scale voxel feature aggregation for 3D object detection from LIDAR point clouds," *Sensors*, vol. 20, no. 3, p. 704, 2020.
- [45] J. Deng, S. Shi, P. Li, W. Zhou, Y. Zhang, and H. Li, "Voxel r-cnn: Towards high performance voxel-based 3d object detection," in *Proceedings of the AAAI Conference on Artificial Intelligence*, vol. 35, no. 2, 2021, pp. 1201–1209.
- [46] Q. Xia, Y. Chen, G. Cai, G. Chen, D. Xie, J. Su, and Z. Wang, "3-D HANet: A Flexible 3-D Heatmap Auxiliary Network for Object Detection," *IEEE Transactions on Geoscience and Remote Sensing*, vol. 61, pp. 1–13, 2023.
- [47] S. Shi, C. Guo, L. Jiang, Z. Wang, J. Shi, X. Wang, and H. Li, "Pv-rnn: Point-voxel feature set abstraction for 3d object detection," in *Proceedings of the IEEE/CVF Conference on Computer Vision and Pattern Recognition*, 2020, pp. 10 529–10 538.
- [48] S. Shi, Z. Wang, J. Shi, X. Wang, and H. Li, "From points to parts: 3d object detection from point cloud with part-aware and part-aggregation network," *IEEE transactions on pattern analysis and machine intelligence*, vol. 43, no. 8, pp. 2647–2664, 2020.
- [49] Y. Hu, Z. Ding, R. Ge, W. Shao, L. Huang, K. Li, and Q. Liu, "Afdetv2: Rethinking the necessity of the second stage for object detection from point clouds," in *Proceedings of the AAAI Conference on Artificial Intelligence*, vol. 36, no. 1, 2022, pp. 969–979.
- [50] Y. Chen, Y. Li, X. Zhang, J. Sun, and J. Jia, "Focal Sparse Convolutional Networks for 3D Object Detection," in *Proceedings of the IEEE/CVF Conference on Computer Vision and Pattern Recognition*, 2022, pp. 5428–5437.
- [51] S. Vora, A. H. Lang, B. Helou, and O. Beijbom, "Pointpainting: Sequential fusion for 3d object detection," in *Proceedings of the IEEE/CVF conference on computer vision and pattern recognition*, 2020, pp. 4604–4612.
- [52] Y. Chen, S. Liu, X. Shen, and J. Jia, "Fast point r-cnn," in *Proceedings of the IEEE/CVF international conference on computer vision*, 2019, pp. 9775–9784.
- [53] X. Bai, Z. Hu, X. Zhu, Q. Huang, Y. Chen, H. Fu, and C.-L. Tai, "Transfusion: Robust lidar-camera fusion for 3d object detection with transformers," in *Proceedings of the IEEE/CVF Conference on Computer Vision and Pattern Recognition*, 2022, pp. 1090–1099.
- [54] Y. Wang, V. C. Guizilini, T. Zhang, Y. Wang, H. Zhao, and J. Solomon, "Detr3d: 3d object detection from multi-view images via 3d-to-2d queries," in *Conference on Robot Learning*. PMLR, 2022, pp. 180–191.
- [55] P. Gao, M. Zheng, X. Wang, J. Dai, and H. Li, "Fast convergence of detr with spatially modulated co-attention," in *2021 IEEE/CVF International Conference on Computer Vision (ICCV)*, Oct 2021. [Online]. Available: <http://dx.doi.org/10.1109/iccv48922.2021.00360>
- [56] Z. Yang, Y. Sun, S. Liu, and J. Jia, "3dssd: Point-based 3d single stage object detector," in *Proceedings of the IEEE/CVF conference on computer vision and pattern recognition*, 2020, pp. 11 040–11 048.
- [57] C. Chen, Z. Chen, J. Zhang, and D. Tao, "Sasa: Semantics-augmented set abstraction for point-based 3d object detection," *Proceedings of the AAAI Conference on Artificial Intelligence*, pp. 221–229, Jul 2022. [Online]. Available: <http://dx.doi.org/10.1609/aaai.v36i1.19897>
- [58] Q. Chen, L. Sun, Z. Wang, K. Jia, and A. Yuille, "Object as hotspots: An anchor-free 3d object detection approach via firing of hotspots," *Cornell University - arXiv,Cornell University - arXiv*, Dec 2019.
- [59] J. Wang, S. Lan, M. Gao, and L. S. Davis, "Infofocus: 3d object detection for autonomous driving with dynamic information modeling," in *European Conference on Computer Vision*. Springer, 2020, pp. 405–420.
- [60] S. Deng, Z. Liang, L. Sun, and K. Jia, "Vista: Boosting 3d object detection via dual cross-view spatial attention," in *Proceedings of the IEEE/CVF Conference on Computer Vision and Pattern Recognition*, 2022, pp. 8448–8457.
- [61] Y. Li, Y. Chen, X. Qi, Z. Li, J. Sun, and J. Jia, "Unifying Voxel-based Representation with Transformer for 3D Object Detection," *arXiv preprint arXiv:2206.00630*, 2022.
- [62] Y. Chen, J. Liu, X. Zhang, X. Qi, and J. Jia, "Largekernel3d: Scaling up kernels in 3d sparse cnns," in *Proceedings of the IEEE/CVF Conference on Computer Vision and Pattern Recognition*, 2023, pp. 13 488–13 498.
- [63] H. Yang, W. Wang, M. Chen, B. Lin, T. He, H. Chen, X. He, and W. Ouyang, "Pvt-ssd: Single-stage 3d object detector with point-voxel transformer," in *Proceedings of the IEEE/CVF Conference on Computer Vision and Pattern Recognition*, 2023, pp. 13 476–13 487.
- [64] W. Xiao, Y. Peng, C. Liu, J. Gao, Y. Wu, and X. Li, "Balanced Sample Assignment and Objective for Single-Model Multi-Class 3D Object Detection," *IEEE Transactions on Circuits and Systems for Video Technology*, 2023.
- [65] J. Deng, W. Zhou, Y. Zhang, and H. Li, "From multi-view to hollow-3D: Hallucinated hollow-3D R-CNN for 3D object detection," *IEEE Transactions on Circuits and Systems for Video Technology*, vol. 31, no. 12, pp. 4722–4734, 2021.
- [66] Z. Li, Y. Yao, Z. Quan, W. Yang, and J. Xie, "Sienet: Spatial information enhancement network for 3d object detection from point cloud," *Cornell University - arXiv,Cornell University - arXiv*, Mar 2021.
- [67] C. He, R. Li, S. Li, and L. Zhang, "Voxel Set Transformer: A Set-to-Set Approach to 3D Object Detection from Point Clouds," in *Proceedings of the IEEE/CVF Conference on Computer Vision and Pattern Recognition*, 2022, pp. 8417–8427.
- [68] Z. Liu, X. Zhao, T. Huang, R. Hu, Y. Zhou, and X. Bai, "Tanet: Robust 3d object detection from point clouds with triple attention," in *Proceedings of the AAAI Conference on Artificial Intelligence*, vol. 34, no. 07, 2020, pp. 11 677–11 684.
- [69] S. Shi, L. Jiang, J. Deng, Z. Wang, C. Guo, J. Shi, X. Wang, and H. Li, "Pv-rnn+: Point-voxel feature set abstraction with local vector representation for 3d object detection," *International Journal of Computer Vision*, vol. 131, no. 2, pp. 531–551, 2023.
- [70] X. Tian, M. Yang, Q. Yu, J. Yong, and D. Xu, "MedoidsFormer: A Strong 3D Object Detection Backbone by Exploiting Interaction with Adjacent Medoid Tokens," *IEEE Transactions on Circuits and Systems for Video Technology*, 2023.
- [71] H. Sheng, S. Cai, Y. Liu, B. Deng, J. Huang, X.-S. Hua, and M.-J. Zhao, "Improving 3d object detection with channel-wise transformer," in *Proceedings of the IEEE/CVF International Conference on Computer Vision*, 2021, pp. 2743–2752.
- [72] Y. Zhang, D. Huang, and Y. Wang, "Pc-rgnn: Point cloud completion and graph neural network for 3d object detection," *Cornell University - arXiv,Cornell University - arXiv*, May 2021.
- [73] J. S. Hu, T. Kuai, and S. L. Waslander, "Point density-aware voxels for lidar 3d object detection," in *Proceedings of the IEEE/CVF conference on computer vision and pattern recognition*, 2022, pp. 8469–8478.
- [74] O. Team *et al.*, "Openpcdet: An open-source toolbox for 3d object detection from point clouds," 2020.



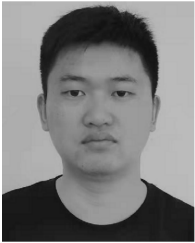
Lin Liu was born in Jinzhou, Liaoning Province, China, in 2001. He received his bachelor's degree from China University of Geosciences(Beijing). Now, he is studying for his master's degree at the Beijing Jiaotong University (China). His research interests are in computer vision.



Lei Yang (Graduate Student Member, IEEE) received his B.E. degree from Taiyuan University of Technology, Taiyuan, China, and the M.S. degree from the Robotics Institute at Beihang University, in 2018. Then he joined the Autonomous Driving R&D Department of JD.COM as an algorithm researcher from 2018 to 2020. He is now a Ph.D. student in the School of Vehicle and Mobility at Tsinghua University since 2020. His current research interests include computer vision, 3D scene understanding and autonomous driving.



Ziying Song was born in Xingtai, Hebei Province, China, in 1997. He received his B.S. degree from Hebei Normal University of Science and Technology (China) in 2019. He received a master's degree from Hebei University of Science and Technology (China) in 2022. He is now a Ph.D. student majoring in Computer Science and Technology at Beijing Jiaotong University (China), with research focus on Computer Vision.



Qiming Xia is currently pursuing the master's degree with the Computer Engineering College, Jimei University, Xiamen, China, in 2013.

His research interests include 3-D object detection of point clouds, machine learning, deep learning theory and its application, knowledge graph, and image processing.



Feiyang Jia was born in Yinchuan, Ningxia Province, China, in 1998. He received his B.S. degree from Beijing Jiaotong University (China) in 2020. He received a master's degree from Beijing Technology and Business University (China) in 2023. He is now a Ph.D. student majoring in Computer Science and Technology at Beijing Jiaotong University (China), with research focus on Computer Vision.



Hongyu Pan received the B.E. degree from Beijing Institute of Technology (BIT) in 2016 and the M.S. degree in computer science from the Institute of Computing Technology (ICT), University of Chinese Academy of Sciences (UCAS), in 2019. He is currently an employee at Horizon Robotics. His research interests include computer vision, pattern recognition, and image processing. He specifically focuses on 3D detection/segmentation/motion and depth estimation.



Caiyan Jia was born in 1976. She received her Ph.D. degree from Institute of Computing Technology, Chinese Academy of Sciences, China, in 2004. She had been a postdoctor in Shanghai Key Lab of Intelligent Information Processing, Fudan University, Shanghai, China, in 2004–2007. She is now a professor in School of Computer and Information Technology, Beijing Jiaotong University, Beijing, China. Her current research interests include deep learning in computer vision, graph neural networks and social computing, etc.